ECOHYDROLOGY
Ecohydrol. **7**, 242–257 (2014)
Published online 24 October 2012 in Wiley Online Library
(wileyonlinelibrary.com) DOI: 10.1002/eco.1333

A geomorphic perspective on terrain-modulated organization of vegetation productivity: analysis in two semiarid grassland ecosystems in Southwestern United States

Javier H. Flores Cervantes,[1]* Erkan Istanbulluoglu,[1] Enrique R. Vivoni,[2]
Chandra D. Holifield Collins[3] and Rafael L. Bras[4]

[1] *Department of Civil and Environmental Engineering, University of Washington, Seattle, WA, 98195, USA*
[2] *School of Earth and Space Exploration and School of Sustainable Engineering and the Built Environment, Arizona State University, Tempe, AZ, 85287, USA*
[3] *Southwest Watershed Research Centre, Agricultural Research Service, USDA, Tucson, AZ, 85719, USA*
[4] *School of Civil and Environmental Engineering and School of Earth and Planetary Sciences, Georgia Institute of Technology, Atlanta, GA 30332, USA*

ABSTRACT

Spatial patterns of ecosystem productivity arise from the terrain-modulated wetting and drying of the landscape. Using a daily relative greenness (*rG*) index, we explore the relations between spatial variability of plant productivity and landscape morphology, and how these relations change over time. The *rG* index is defined as a measure of local vegetation greenness relative to the site's mean greenness, calculated from remotely sensed normalized difference vegetation index. We analyse two semiarid grasslands with pronounced topography, one located in southeastern Arizona, with a mean annual precipitation of 350 mm, and the other in central New Mexico, with a mean annual precipitation of 250 mm. Our results indicate that (1) *rG* is spatially more uniform after wet conditions (higher biomass) than after dry conditions (lower biomass); (2) differences in the relative frequency distribution of *rG* among different landscape morphologies (ridges, unchanneled valleys and channels) indicate higher productivity in channels, similar coefficient of variation in all process domains, and higher skewness in the ridges; (3) relatively high correlations between the binned average *rG* with respect to upstream area, curvature, and annual insolation in more than 80% of the terrain indicate a clear dependence between ecosystem productivity and topography; (4) *rG* is more sensitive to changes in topographic indices at the wetter Arizona study site. Such improved understanding of vegetation-topography dependence is critical for ecosystem management, testing ecohydrologic models, and offers ideas for the downscaling of coarse-scale satellite-derived vegetation indices. Copyright © 2012 John Wiley & Sons, Ltd.

KEY WORDS geomorphology; productivity; grassland; topography

Received 30 April 2012; Revised 17 September 2012; Accepted 17 September 2012

INTRODUCTION

Ecosystem patterns and productivity on the landscape are mainly driven by the amount and distribution of solar radiation, air temperature and soil moisture (Eagleson, 2002; Larcher, 2003; Bonan, 2008). These factors are defined by climate at a regional scale and mediated by topography and soil properties at a local scale, leading to spatial vegetation patterns at the watershed scale (Hack and Goodlett, 1960; Ivanov *et al*., 2008; Hwang *et al*., 2009).

The role of topography on vegetation distribution has been discussed in the literature since the work of Hack and Goodlett (1960). More recently, digital elevation models (DEMs) have prompted detailed spatial analysis of associations between ecosystem properties and variables describing landscape morphology (Florinsky and Kuryakova, 1996; Hwang *et al*., 2009; Riveros-Iregui and McGlynn, 2009; Svoray and Karnieli, 2010; Yetemen *et al*., 2010). The landscape variables often used in such studies are local slope (*S*), total curvature (*Curv*), aspect (*Asp*) and upstream contributing area (*UA*), which impact soil moisture and ecosystem productivity on the landscape. Of these, *S*, *Asp* and *Curv* are local variables and are calculated using the elevation of a given point and its neighbours. *S* influences the subsurface and surface flow velocity. *S* and *Asp* together influence local rainfall input and radiation influx (Sharon, 1980). *Curv* is the sum of planform and profile curvatures, and provides an overall measure of landscape convergence/divergence (Zevenbergen and Thorne, 1987; Western *et al*., 1999). Besides these topographic variables, in steep terrain and at spatial scales of mountain ranges, elevation and landscape relief often have strong controls on both temperature and precipitation (Whiteman, 2000). Those larger spatial scale effects are not the focus of this paper. This paper concentrates on relatively low-relief landscapes and smaller spatial scales of the order of a couple to tens of squared kilometres.

Aspect-driven differences on vegetation productivity have been the focus of a number of studies arguing that vegetation growth is favoured on northern aspects receiving less solar radiation (Hidalgo *et al*., 1990; Kirkby *et al*., 1990; Gutiérrez-Jurado *et al*., 2006; Istanbulluoglu *et al*., 2008). For example, in four different sites in a mountainous region in

*Correspondence to: Javier H. Flores Cervantes, Department of Civil and Environmental Engineering, University of Washington, Seattle, WA 98195. E-mail: homefc@uw.edu

eastern Kazakhstan (precipitation of 500–2000 mm/year), Florinsky and Kuryakova (1996) found relations between aspect and plant types in sites with insignificant human impact, where forests on northern aspects gradually shift to more xeric plant types (bushes and shrubby steppe) on southern aspects. In central New Mexico, ecotone shifts from a tree-grass savanna ecosystem on north-facing slopes to a shrub landscape on south-facing slopes can be observed over distances of several tens of metres in valleys with moderate topography (~30–40 m hillslope relief) (Gutiérrez-Jurado *et al.*, 2006; Istanbulluoglu *et al.*, 2008).

Using a numerical model that resolves water and energy coupling on the landscape, Ivanov *et al.* (2008) predicted higher vegetation productivity on north-facing slopes, convergent topography and in channels, and lower productivity on south-facing slopes and diverging landscape positions for central New Mexico. Interestingly, in their model simulations, whereas vegetation growth on south-facing terrain was mainly limited because of excess solar radiation, vegetation growth on steep north-facing terrain was limited by 'rainfall insufficiency', caused by the reduction of the amount of intercepted rain on steep slopes (Ivanov *et al.*, 2008).

The role of *UA* in vegetation productivity and ecosystem patterns has also been recognized across a range of climates. In a lodgepole-dominated subalpine mountainous watershed (precipitation of 880 mm/year, 70% snow) in central Montana, Riveros-Iregui and McGlynn (2009) reported positive linear dependence of soil respiration rate and root density and *UA*, and attributed this to wetter conditions due to lateral redistribution of soil moisture as watershed area grows. Furthermore, the sensitivity of respiration to changes in *UA* was stronger in southeastern slopes than that in northern aspects (Riveros-Iregui and McGlynn, 2009).

Hwang *et al.* (2009) studied watershed-scale ecosystem processes in a marine, humid temperate climate (precipitation of 1870–2500 mm/year) in the Coweeta Hydrologic Lab, North Carolina. Despite the humid climate, topography-driven variations in soil moisture were found to strongly control vegetation density and modelled nitrogen availability along topographic wetness index gradients. Greater nutrient availability as a result of a more rapid cycling of organic matter with growing wetness mediated by topography has also been documented earlier in the site (Knoepp and Swank, 1998; Knoepp *et al.*, 2008).

Svoray and Karnieli (2010) addressed vegetation variability from a geomorphic perspective in a hilly region with an ephemeral stream in Northern Negev, Israel (precipitation of 270 mm/year, winter season) using normalized difference vegetation index (NDVI) maps during the 2002–2003 growing season. Hillslopes were characterized with respect to five pedogeomorphic units starting from the hillcrest in the following order: interfluve, shoulder, backslope, footslope and channel. In most days during green-up, NDVI was found to be statistically different among different topographic positions, with lowest NDVI in interfluves and highest NDVI in channels. Because of both thicker soil reservoirs and larger run-on contributions, footslopes and channels had the most different NDVI compared with other pedogeomorphic units.

The observed associations between ecosystem properties and watershed topographic indices discussed previously are strongly related to the spatial patterns and dynamics of soil moisture across the landscape, mediated by climate fluctuations and seasonality (Western *et al.*, 1999; Blöschl and Grayson, 2001). A prime example of this was presented by Western *et al.* (1999) in the Tarrawarra catchment (10.5 ha), Australia, where the spatial patterns of soil moisture were measured across the basin (>500 points) over a growing season. The spatial organization of soil moisture changed with time and was correlated best with distinct topographic indices at different times of the rainy season. During the initial wetting phase, soil moisture was better correlated with local curvature, implying local water convergence. As wetting continued, moisture extended to the channels and outlet of the watershed, and soil moisture was better correlated with *UA*. During the drying phase of the watershed, spatial patterns of soil moisture were better correlated with potential radiation index, because of radiation's regulation on evapotranspiration. The potential radiation index is the ratio of potential solar radiation (i.e. in the absence of atmosphere) on a sloping surface to that on a horizontal surface. Under dry and extremely wet conditions, soil moisture organization was muted as the landscape connectivity and radiation forcing played a reduced role (Western *et al.*, 1999). Such improved understanding of the dominant seasonal topographic controls on the organizational and statistical characteristics of soil moisture within a watershed has contributed to the predictive theory of the integrated watershed behaviour in hydrology (Dunne and Black, 1970; Dunne *et al.*, 1975; Beven and Kirkby, 1979; Moore *et al.*, 1988; Western *et al.*, 1999; Willgoose and Perera, 2001).

Vegetation has longer-term memory than soil moisture as an ecosystem has the capacity to store water, carbon and nitrogen in various pools that can last longer than a typical drying cycle of soil moisture (i.e. a few days) (e.g. Schwinning *et al.*, 2004). Thus, in semiarid regions, the spatial patterns of vegetation could be more stable than soil moisture patterns. Given that topography dictates the moisture spatial distribution, it leads to niches of vegetation productivity (Noy-Meir, 1973). Understanding the structure and degree of spatial and temporal organization of vegetation type and productivity is critical for improved predictions of the landscape-scale ecohydrologic responses to disturbances and climate change.

The studies reviewed previously have shown dependencies between vegetation attributes (type, productivity, fluxes) and topographic variables. However, little is known about how the topographic controls on vegetation dynamics change over time in relation to climate seasonality and its interannual variability. In this study, we address this question in two semiarid ecosystems of the Southwestern United States. We recognize that local topographic variables (*S*, *Curv*, *Asp*) organize in relation to *UA* in landscapes (e.g., Yetemen *et al.*, 2010), which may warrant a multivariable landscape analysis. Following the work of Svoray and Karnieli (2010), we take a geomorphic perspective and investigate the relations between vegetation properties and terrain indices in different geomorphic process domains (ridges, unchanneled valleys and channels), addressing the following questions: (1) How different is the spatial variability of vegetation within different geomorphic process domains? (2) How does vegetation

productivity change along topographic gradients of *UA* and *Curv*? (3) How significant is the role of terrain-modulated radiation on vegetation productivity? and (4) What is the combined effect of these topographic variables on vegetation productivity? In the following section, we proceed with describing the methods used for delineating geomorphic process domains and the calculation of local solar radiation. Next we present our field sites, data analyses and results.

METHODS

Quantitative measures of catchment morphology

A process domain represents a portion of a catchment where a certain type of erosion process is dominant and shapes the landscape over time (e.g. Montgomery, 1999). We used the observed slope–upstream area (*S–UA*) and curvature–upstream area (*Curv–UA*) relations to stratify the landscape into distinct process domains with different morphologies along a *UA* gradient. These relations emerge from and characterize the geomorphic signature of the dominant forms of erosion processes on the landscape.

Slope–area relation. A power–law relation between the local slope of a given point on the landscape (S) and its *UA* of the general form $S = k \cdot UA^{\theta}$ is widely observed in natural landscapes. This power–law has been extensively used to characterize the change in S along water flow paths from the interfluves to the outlet of a basin. The general form of the *S–UA* relation has been related to the competition between S dependent processes (soil creep, dry landsliding) that cause terrain steepening with *UA* (convex profile, positive θ) to enhance slope-dependent transport (under a given uplift), and the S and *UA* dependent (water-driven) erosion processes that carve valleys as *UA* grows, leading to a concave valley profile (negative θ). In the transition zone between rounded convex ridges to concave valleys (backslope), the power–law relationship is not observed. This region is characterized by an inflexion point on the *S–UA* relation and represents the valley head (VH), where the steepest slopes along the *UA* gradient are found. The transition between concave valleys and channels is typically marked by a decrease in the value of θ (Istanbulluoglu *et al.*, 2008). In channels, k and θ are referred to as the steepness index and the concavity index, respectively. The concavity index is the gradient (degree of steepness) of the slope–area (*S–UA*) relation in a log–log plot ($\log(S) = \log(k) + \theta \log(\boldsymbol{UA})$).

The role of uplift and erosion rates (Willgoose *et al.*, 1991; Tarboton *et al.*, 1992; Wobus *et al.*, 2006), erosion thresholds and substrate size (Tucker and Bras, 1998; Gasparini *et al.*, 2004), variable climatology (Sólyom and Tucker, 2004) and vegetation (Collins *et al.*, 2004; Istanbulluoglu and Bras, 2005) on the *S–UA* relation have been theoretically examined in the literature. In fluvial valleys, most θ values fall in the range between -0.4 and -0.7 (Howard, 1980; Tarboton *et al.*, 1992).

Curvature–area relation. Corollary to the *S–UA* relation, curvature (i.e. Laplacian of elevation z, $\nabla^2 z$) is another useful measure for the interpretation of sediment transport processes (Bogaart and Troch, 2006; Istanbulluoglu *et al.*, 2008; Tarolli and Dalla Fontana, 2009; Gutiérrez-Jurado and Vivoni, 2011). *Curv* is defined as the sum of planform ($\partial^2 z/\partial x^2$) and profile ($\partial^2 z/\partial y^2$) curvatures (Moore *et al.*, 1991):

$$\nabla^2 z = \left(\frac{\partial^2 z}{\partial x^2} + \frac{\partial^2 z}{\partial y^2}\right) \tag{1}$$

Profile curvature indicates the degree of convexity or concavity of the terrain along flow paths and is similar to the concavity index of the *S–UA* relation. Planform curvature represents the degree of local convergence or divergence on the landscape. Thus, *Curv* provides a comprehensive measure of the degree of local moisture and sediment convergence. In general terms, divergent-convex ridges ($\nabla^2 z < 0$) are formed under the dominant control of slope-dependent sediment transport processes, whereas convergent–concave valleys and channels ($\nabla^2 z > 0$) result from the dominant control of water-driven erosion. As a result, total curvature tends to be positive where $\theta > 0$ and negative where $\theta < 0$, with a transition between convergent and divergent zones at the VH (Istanbulluoglu *et al.*, 2008).

Incoming solar radiation

Annual incoming solar radiation (*Rad*) indicates the amount of available solar energy on the landscape and is used as another topographic variable to explain vegetation observations. *Rad* is calculated by integrating the instantaneous shortwave clear-sky radiation (R_d) received on the terrain throughout a year. R_d depends on several factors: the geographic location defined by latitude, the day of the year, the time of the day, and S and *Asp* (see APPENDIX for details). In this paper, *Rad* is estimated by calculating R_d at 6-min intervals and adding them throughout the calendar year. Our estimates do not account for the contribution of diffuse radiation, most relevant during cloudy conditions or topographic shadowing effects. But these are not major concerns given that the study sites are characterized by cloudless conditions the majority of the year, and terrain is gentle enough so that shadowing effects are minimal.

We illustrate the distribution of *Rad* as a function of S and *Asp* for the location of our southeastern Arizona study site at latitude 32°N in Figure 1. At this latitude, *Rad* peaks at intermediate values of S in the 20° to 30° range on south-facing aspects and is minimum in steep north-facing terrain ($S > 30°$). The range of plotted *Rad* in the figure (3 to 8 GJ/m^2) correspond to 1226 to 3448 mm of water equivalent that could have significant implications on regional ecohydrology.

An interesting feature of the *Rad* field is regions of equal annual radiation for different combinations of slopes and aspects. For example, *Rad* of 6.5 GJ/m^2 occurs in north-facing (*Asp* is 0°) terrain with a slope of 15°, and in east and west facing terrain (*Asp* are 90° and 270°, respectively) under a 35° slope. This suggests similarity in potential evapotranspiration on the landscape, conditioned on local slope and aspect. In Figure 1, a steep east/west facing surface and a gentler north-facing surface both have an identical

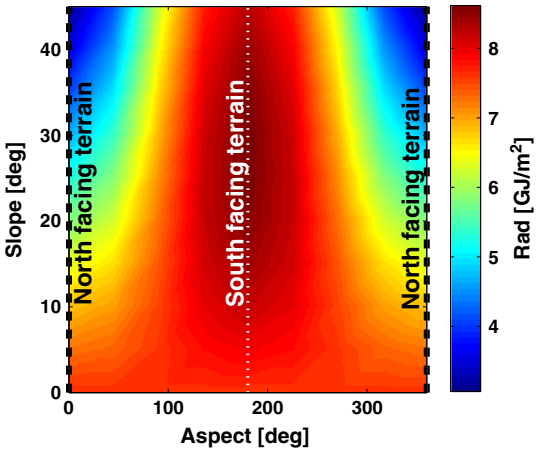

Figure 1. Annual solar radiation (*Rad*) for 32°N corresponding to one of our study sites in southeastern Arizona, USA as a function of aspect and slope. Exact south aspect (*Asp*) is at 180°, and north *Asp* corresponds to 0° and 360°.

Rad and thus are expected to have similar potential evapotranspiration demands.

FIELD SITES AND DATA

Field sites

This study focuses on two semiarid ecosystems located in southeastern Arizona and in central New Mexico. These two study sites are selected for their pronounced topography, similar occurrence of herbaceous (grass) cover, and slight differences in their annual precipitation, providing an opportunity to examine the sensitivity of spatial patterns to precipitation under a generally similar desert climate.

The first site is the Kendall catchment located in the headwaters of the Walnut Gulch Experimental Watershed (Figure 2(a)), with an area of ~4 km^2, underlain by alluvial fan deposits (1500–1600 m a.m.s.l). We refer to this site as the AZ site in the reminder of the paper. The mean annual precipitation, temperature and pan evaporation are 350 mm, 17.7°C and 2590 mm, respectively, with temporal distributions affected by strong seasonality. Two-thirds of the annual precipitation falls during the North American Monsoon (NAM) from July to September, and mean monthly temperatures range between 8°C in January and 27°C in July. Vegetation is dominated by C4 perennial grasses, including black, blue, hairy and sideoats gramas (*Bouteloua eripoda*, *B. gracilis*, *B. hirsuta* and *B. curtipendula*) (Nouvellon *et al.*, 2001).

The second site is a 10 km × 12 km area located in the northwestern portion of the Sevilleta National Wildlife Refuge (SNWR) in central NM (Figure 2(a,b)), referred to as the NM site. This site is part of the NSF Long Term Ecological Research network. The mean annual precipitation is 250 mm, more than 50% of it falls during the NAM. Mean monthly temperatures range between 2.5°C in January and 25°C in July. Elevation ranges between 1450 and 2500 m a.m.s.l, and the surface consists of deposits of various sources including alluvial and eolian sand, and terraces with coarse soil textures.

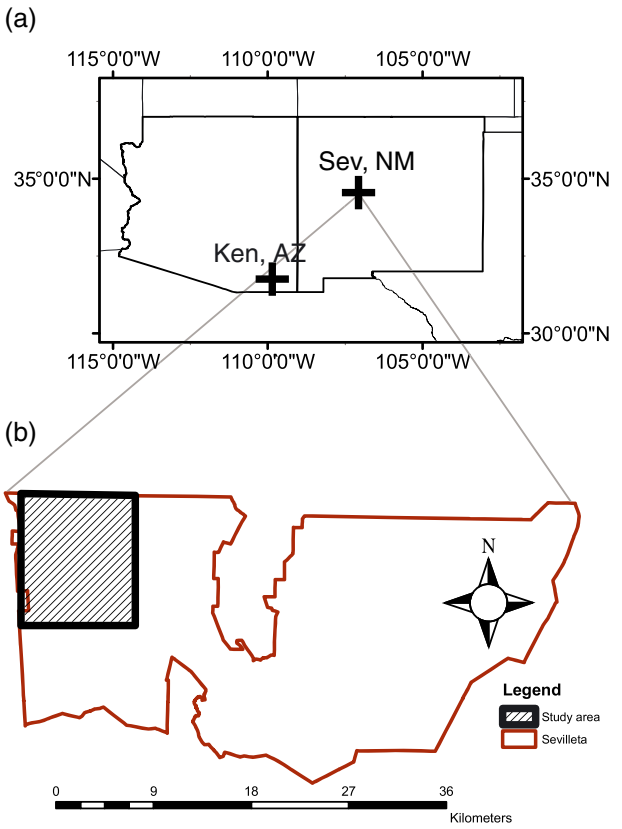

Figure 2. (a) Location maps of our study sites in southeastern AZ and central NM; (b) the central NM study site: northwest corner of the Sevilleta National Wildlife Refuge.

The region is covered with grasslands and shrublands, and coniferous woodlands and forests at higher elevations. For this study, only the terrain dominated by grass species was considered, which consists of 50% of the total area selected. The grass species extent was determined on the basis of the vegetation classification map of Muldavin *et al.* (1998). Grass species include black and blue grama (Gutiérrez-Jurado *et al.*, 2007). In these ecosystems, most biomass production occurs during and shortly after the NAM, with occasional spring growth resulting from winter accumulated moisture in the soil (Notaro *et al.*, 2010).

Data

We use remotely sensed data to quantify the spatial variability of aboveground plant productivity in both sites. For the AZ site, we use the NDVI directly. For the NM site, we use available biomass estimates calculated from NDVI data by Shore and Gosz (2002), on the basis of linear relationships between Landsat NDVI data and field-measured biomass at certain locations in the SNWR.

In the AZ site, we use five NDVI fields corresponding to the growing period (July to October) between 1990 and 1999, with a spatial resolution of 30 m. The data were derived from NASA's Landsat Thematic Mapper images, geocorrected to subpixel accuracy and corrected for atmospheric conditions using the refined empirical line method (Holifield *et al.*, 2003). In the NM site, we use 22 maps of biomass, corresponding to the growing period (April to October), encompassing 17 years

(1984–2001). The data had a spatial resolution of 28.5 m until 1999 and 30 m after 1999, because of changes in the satellite instruments used. The data were publicly available from the Sevilleta Long Term Ecological Research website (http://sev.lternet.edu/).

Landscape morphology is represented by DEMs, which are used to derive the local *S*, *Asp*, *UA* and *Curv* fields in the basins. In the AZ site, a 1-m resolution laser altimetry DEM was provided by the US Department of Agriculture, Agricultural Research Station. To be more consistent with the NDVI resolution, these data were aggregated to a 10 m DEM. In the NM site, we use a 10 m DEM derived from Interferometric Synthetic Aperture Radar, available at http://sev.lternet.edu/. The availability of high-resolution DEMs allowed us to compute all topographic indices more accurately at a 10 m resolution. To characterize the vegetation biomass corresponding to each 10-m DEM cell, we use the biomass of the overlapping 30-m biomass pixel.

Relative vegetation productivity

The focus of this study is to examine the spatial variability of vegetation. Therefore, an index that quantifies the relative differences in grass productivity in space is needed. For this purpose, a relative measure of local greenness with respect to the mean state of the area, *rG*, is defined as the ratio of a local aboveground biomass to the spatial mean biomass for a given day. In the NM site, this is

$$rG_i^t = \frac{biomass_i^t}{\overline{biomass^t}} \tag{2}$$

whereas the AZ site uses NDVI instead of biomass such that *rG* is given as

$$rG_i^t = \frac{NDVI_i^t}{\overline{NDVI^t}} \tag{3}$$

where *i* indicates pixel location, *t* indicates time (day and year) and the overbar represents the spatial mean of the NDVI and biomass fields for a given day *t*. Daily *rG* fields in both sites were calculated using each of the 5 days of the NDVI fields in the AZ site and 22 days of the biomass fields in the NM site. To characterize the mean seasonal spatial vegetation patterns, we calculate the time-averaged *rG* fields, *TArG*. A *TArG* field is calculated by taking the arithmetic average of rG^t fields, as indicated in Equation (4), where *n* is the number of daily *rG* fields. In the AZ site, $n = 5$, and in the NM site, $n = 22$.

$$TArG_i = \frac{\sum_{t=1}^{n} rG_i^t}{n} \tag{4}$$

To illustrate the spatial variability of biomass, we plot annual radiation (*Rad*) and the time-averaged relative greenness (*TArG*) for the AZ site (Figure 3). Both figures show clear patterns. In Figure 3(a), south-facing slopes receive more *Rad* than north-facing slopes. The spatial variability of

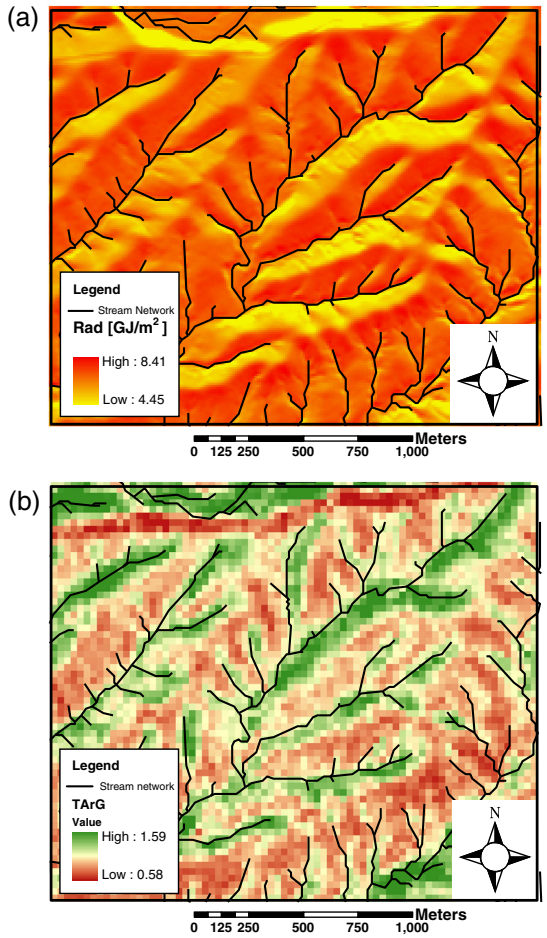

Figure 3. Maps of (a) *Rad* and (b) *TArG* for the AZ site. The channel network in the maps is identified using the 10,000 m^2 *UA* threshold obtained from the *S*–*UA* relation of the catchment (Figure 4(a)).

the solar energy received by the opposing aspects manifests itself on the *TArG* field. Figure 3(b) shows that in south-facing terrain, *TArG* is as low as 0.58, whereas in north-facing terrain, *TArG* is up to 1.5. *TArG* also grows along the channel network.

RESULTS AND DISCUSSION

Geomorphic delineation of the landscape

We begin our analysis by delineating the distinct geomorphic regions along a *UA* gradient over which differences in *rG* and *TArG* are examined. For this purpose, the *S*–*UA* and *Curv*–*UA* relations of both sites are presented (Figure 4). To facilitate comparisons, averages of local *S* and *Curv* for pixels grouped according to an *UA* range are plotted with respect to the midpoint of their respective *UA* range. In the *S*–*UA* plot, three distinct regions are recognized. Region I corresponds to convex rounded ridges (low *UA*) where *S* increases with *UA* ($\theta > 0$). Region II corresponds to concave unchanneled valleys (middle range of *UA*), and region III corresponds to channels (upper range of *UA*). In regions II and III, *S* decreases with *UA* ($\theta < 0$). *S* decreases faster with *UA* in II than III (Istanbulluoglu *et al.*, 2008). The boundary between regions II and III is determined by visual inspection of the *gradient* of the *S*–*UA* relation of the semilog plot in Figure 4(a). The gradient is negative in regions II and III, but it is steeper in region II.

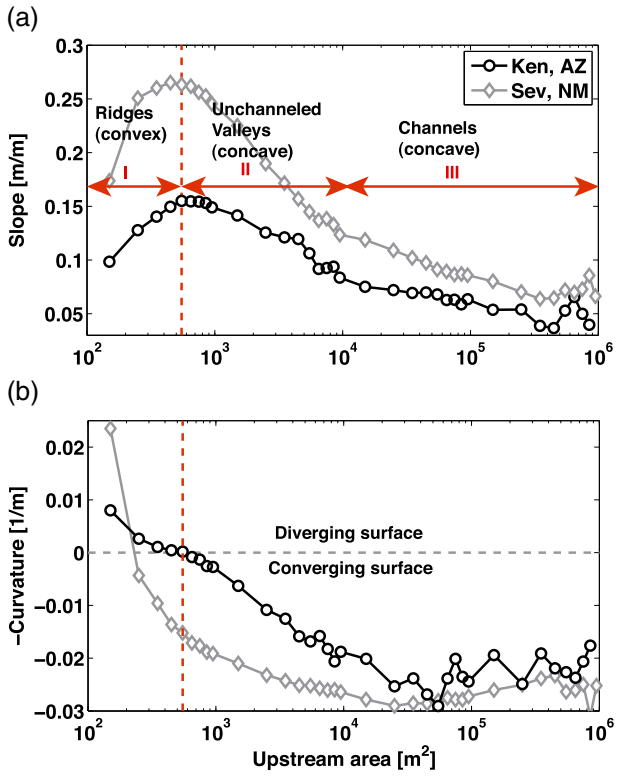

Figure 4. (a) The slope–upstream area and (b) curvature–upstream area relations plotted for the field sites in AZ and NM. The horizontal red arrows designate the approximate extent of regions I, II and II in the slope–upstream area relation, corresponding to ridges, unchanneled valleys and channels.

The link between the change in gradient in the *S–UA* plot and the separation between regions II and III is documented in Istanbulluoglu *et al*. (2008).

In the *S–UA* relation, the ridge–valley transition, often referred to as the VH (e.g., Tarboton *et al*., 1992), occurs with an approximate *UA* of 550 m^2 at the AZ site (designated with a vertical dashed line in Figure 4(a)) and 450 m^2 at the NM site, separating the convex ridges from concave unchanneled valleys. Channels begin at approximately 10,000 m^2 at both study sites. These thresholds have been verified by field observations at the NM site (Gutiérrez-Jurado *et al*., 2007; Istanbulluoglu *et al*., 2008). The NM site is overall steeper than the AZ site, most profoundly along the ride–valley transition zone (VH), leading to a broader range of radiation exposure on landscape elements.

In the AZ site, the change from negative to positive *Curv* (diverging to converging morphology) occurs relatively gradually and with a similar *UA* that marks the VH location in the *S–UA* relation (Figure 4(b)). In the NM site, the transition from divergent to convergent local morphology occurs abruptly, with a smaller *UA*, far upstream of the VH location (Figure 4(b)). This suggests that on average, a concave valley profile forms further downslope of the point where local convergence begins in the NM site. These differences are in agreement with the visual appearance of the sites. In the AZ site, the landscape is composed of moderately sloped rolling hills, whereas the NM site has more dissected terrain with smaller hillslopes and sharper ridges.

To illustrate the organization of different geomorphic process domains, we used the *UA* thresholds identified previously and mapped ridges ($UA \leq 550\ m^2$), unchanneled valleys ($550\ m^2 < UA \leq 10{,}000\ m^2$) and the main channel network ($UA > 10{,}000\ m^2$) at the AZ site (Figure 5(a)). The NM site is not shown because of its larger size. The domains mapped show the organization of valleys around channels, and ridges highlight the separation of valleys. At both sites, ridges account for the majority of the terrain (~70%), followed by unchanneled valleys (~25%). Channels only occupy a small fraction of the basin (~5%). At the AZ site, ~62% of the terrain is divergent, and 38% is convergent (Figure 5(b)). At the NM site, divergent and convergent terrain elements have nearly equal percentages (~41%).

Distribution of vegetation in the landscape

Relative frequency distributions. Before we examine how grassland productivity relates to different landscape form, we illustrate the spatial variability of vegetation cover in both sites by plotting the relative frequency distribution (rfd) of *TArG* (Equation (4)) and *rG* for days with the highest (Max-AB) and lowest (Min-AB) spatial mean biomass (Figure 6(a,b)). The differences between Max-AB and Min-AB would illustrate how spatial variability of vegetation biomass changes with respect to the mean value of the field during high and low biomass conditions (i.e. seasonal effect). At the AZ site, the lowest NDVI value

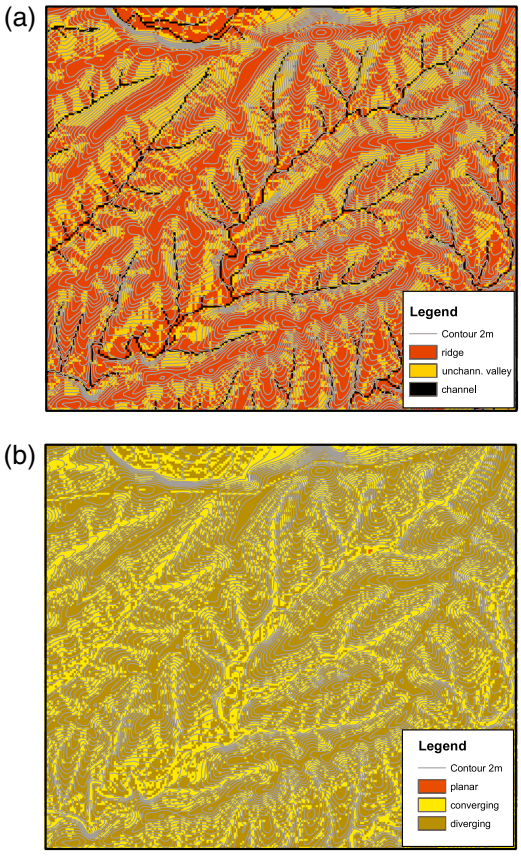

Figure 5. Maps of the geomorphic regions of the AZ site delineated on the basis of the *S–UA* relations of the basin: (a) ridges, valleys and channels; (b) converging and diverging regions.

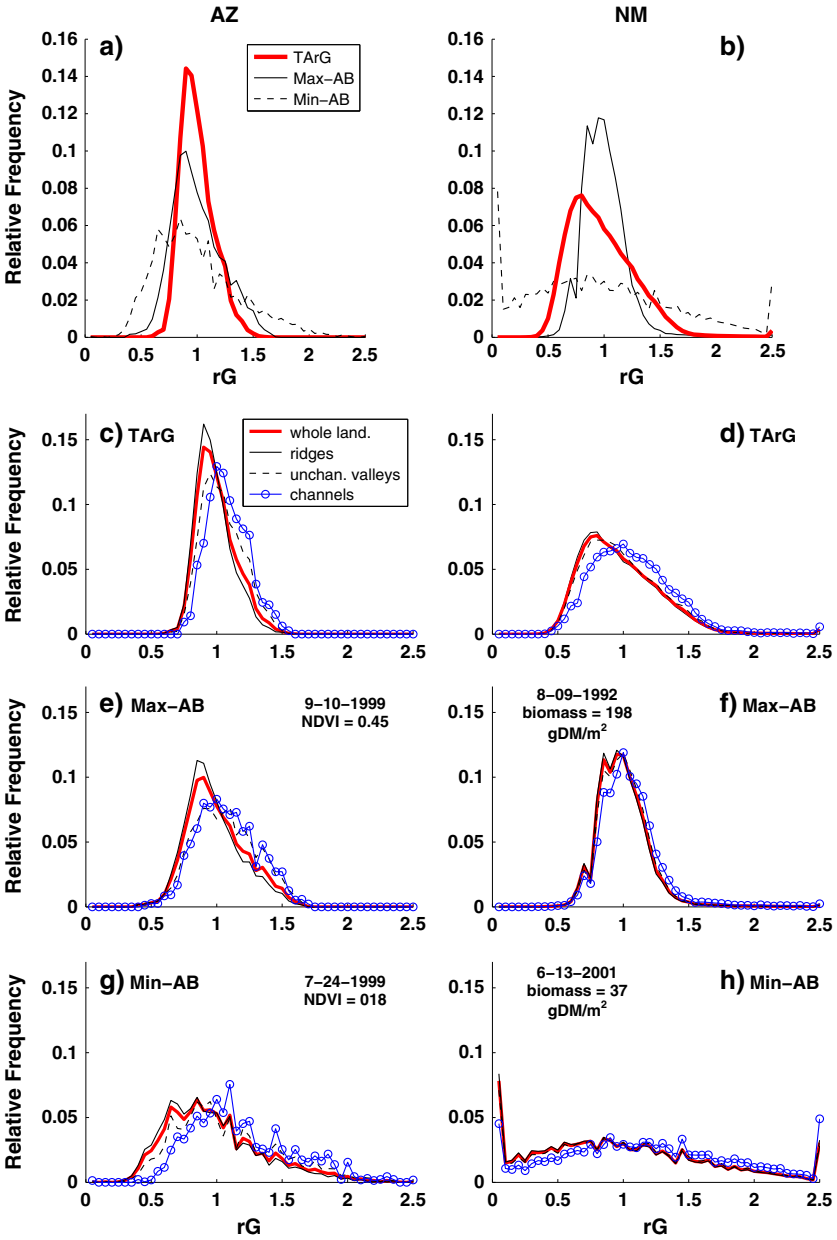

Figure 6. Relative frequency distribution of the time-averaged *rG* (*TArG*), and the *rG*s corresponding to days with maximum aboveground biomass (Max-AB) and minimum aboveground biomass (Min-AB) in the Arizona (a) and New Mexico (b) sites, for the whole landscape and (c–h) for different geomorphic regions (ridges, unchanneled valleys and channels).

was 0.18 on 24 July 1999 (before the 1999 NAM), and the highest NDVI value was 0.45 on 10 September 1999 (after NAM). At the NM site, 09 August 1992 had the highest biomass of the examined period, 198 g DM/m^2, and the lowest value obtained was 37 g DM/m^2 occurring on 13 June 2001. In addition to the rdfs, Tables I and II provide the coefficient of variation (CV), skewness and kurtosis of the data sets corresponding to the rdfs. Table II also provides the mean *rG* for each geomorphic region. The mean *rG* for the whole landscape is 1.

In Figure 6(a,b), regions with $rG > 1$ ($rG < 1$) have higher (lower) biomass than the spatial mean value of the field. The spread of the rdf indicates the variability of the vegetation cover in space. In the NM site, the *TArG* shows more spatial variability than in the AZ site, its CV is twice as large. This higher variability is in agreement with the broader range of slopes and curvatures at the site. The NM site *TArG* distribution also shows large positive skewness and kurtosis, both twice as large as those of the AZ site. The value of kurtosis in NM, twice that of a standard normal distribution ($>>3$), suggests the existence of infrequent extreme variations in local biomass at this site. In contrast, in AZ, the *TArG* distribution shows a nearly bell-shape form with a very narrow base, a small positive skewness and a kurtosis slightly above that of a standard normal distribution (>3).

The rfds for the Max-AB days approach a bell-shape form at both sites, whereas for the Min-AB days, the rfds have reduced peaks and wider bases. In the NM site, for Min-AB (Figure 6(b), 37 g/m^2 on 13 June 2001), the *rG* distribution shows multiple peaks occurring for *rG* slightly less than 1 and at minimum and maximum *rG*s. The minimum *rG* corresponds to nearly bare conditions. The higher local

Table I. Statistics of the *TArG*, Max-AB and Min-AB for the study sites for the whole landscape.

	AZ *TArG*	Max-AB	Min-AB	NM *TArG*	Max-AB	Min-AB
Coefficient of variation	0.15	0.22	0.38	0.31	0.20	0.70
Skewness	0.65	0.46	0.82	1.43	2.09	1.10
Kurtosis	3.23	2.84	3.53	8.13	14.43	6.11

Table II. Statistics of the *TArG*, Max-AB and Min-AB for the study sites for each geomorphic region.

		AZ			NM		
		Ridges	Valleys	Channels	Ridges	Valleys	Channels
TArG	Mean	0.98	1.04	1.08	0.97	1	1.08
	Coefficient of variation	0.14	0.15	0.14	0.31	0.31	0.30
	Skewness	0.72	0.43	0.41	1.48	1.34	1.37
	Kurtosis	3.61	2.70	2.76	8.41	7.78	7.56
Max-AB	Mean	0.97	1.06	1.08	0.99	1.01	1.05
	Coefficient of variation	0.22	0.22	0.21	0.20	0.20	0.22
	Skewness	0.57	0.15	0.20	2.06	2.04	2.08
	Kurtosis	3.16	2.50	2.56	14.51	14.87	12.39
Min-AB	Mean	0.96	1.08	1.19	0.97	1.03	1.20
	Coefficient of variation	0.37	0.37	0.32	0.72	0.69	0.61
	Skewness	0.87	0.70	0.68	1.12	1.10	0.98
	Kurtosis	3.72	3.14	3.33	6.21	6.04	5.78

rG ($>92.5\ g/m^2$) corresponds to localized higher biomass along the valley floors.

The differences in rfds between Max-AB and Min-AB suggest that after favourable conditions for vegetation growth (i.e. after NAM), vegetation spatial distribution is less variable and more symmetrical around the mean than under low biomass conditions (i.e. before the growing season). These findings suggest that under low biomass conditions, when there is a larger spatial variability in *rG*, topography could be playing a more profound role on plant productivity than in wetter conditions.

In Figure 6(c–h), we illustrate the variability of *TArG* and *rG*s for Min-AB (dry season) and Max-AB (wet season) days in different landscape morphologies (ridges, unchanneled valleys and channels). In both sites, from channels to unchanneled valleys and to ridges, for all three biomass conditions (*TArG*, Max-AB and Min-AB), the mode and the mean of the distributions become smaller; the distributions tend to become more positively skewed and peaked (higher kurtosis), whereas their CV remains relatively unchanged. These observations are slightly muted in the NM site where mean annual precipitation is lower. The most profound differences in rfds among the three defined geomorphic regions are between ridges and channels. This indicates a clear control of *UA* in ecosystem productivity. In all biomass cases, the shape of the whole landscape rfd is dominated by ridges because of their larger extent (~70%) in the landscape.

Topographic controls on ecosystem productivity. In the previous sections, we have demonstrated that landscape morphology and seasonality influence the spatial variability of vegetation cover. Differences among geomorphic regions were more pronounced in the AZ site that has a higher mean annual precipitation. These observations lead to the following question: Is there a relationship between local vegetation biomass and topographic indices (*UA*, *Curv*, *S* and *Asp* as they influence *Rad*), and how does this vary with the mean biomass of the field (i.e. in different days in the season or year)? To investigate this, we plot *rG* as a function of *UA*, *Curv* and *Rad* (Figure 7). In the 'Combined effects of lateral redistribution and evapotranspiration on ecosystem' section, we examine the cumulative effect of these variables on *rG*. Here, to facilitate comparisons, we plot the average *rG* calculated for pixels binned and averaged along gradients of each topographic index for each day of the data (including the Min-AB and Max-AB days) and for *TArG*. The size of the bins is different for each topographic index. For *UA*, the bin size is variable; it is set to $100\ m^2$ for the lowest *UA* range and increases by a factor of 10 each time the $\log_{10}$ of *UA* increases by one unit. For *Curv*, the bin size is 0.005 and 0.01 (1/m) for the AZ and NM sites, respectively. For *Rad*, the bin size is assumed constant of $0.25\ GJ/m^2$. In Figure 7, Min-AB and Max-AB days are indicated with black solid and dashed lines, respectively; data for *TArG* are presented with a red thick line, and all other data are presented with grey solid lines.

Upstream area control. Figure 7(a,b) shows the *rG–UA* relation using the binned data. Despite some variations among days, *rG* consistently grows with *UA* in both sites. Such an increase is expected and arguably associated with higher soil moisture accumulation along channels (Gutiérrez-Jurado *et al.*, 2007). Besides the role of *UA* providing more moisture, an interesting connection between the *rG–UA* and geomorphic position emerges in

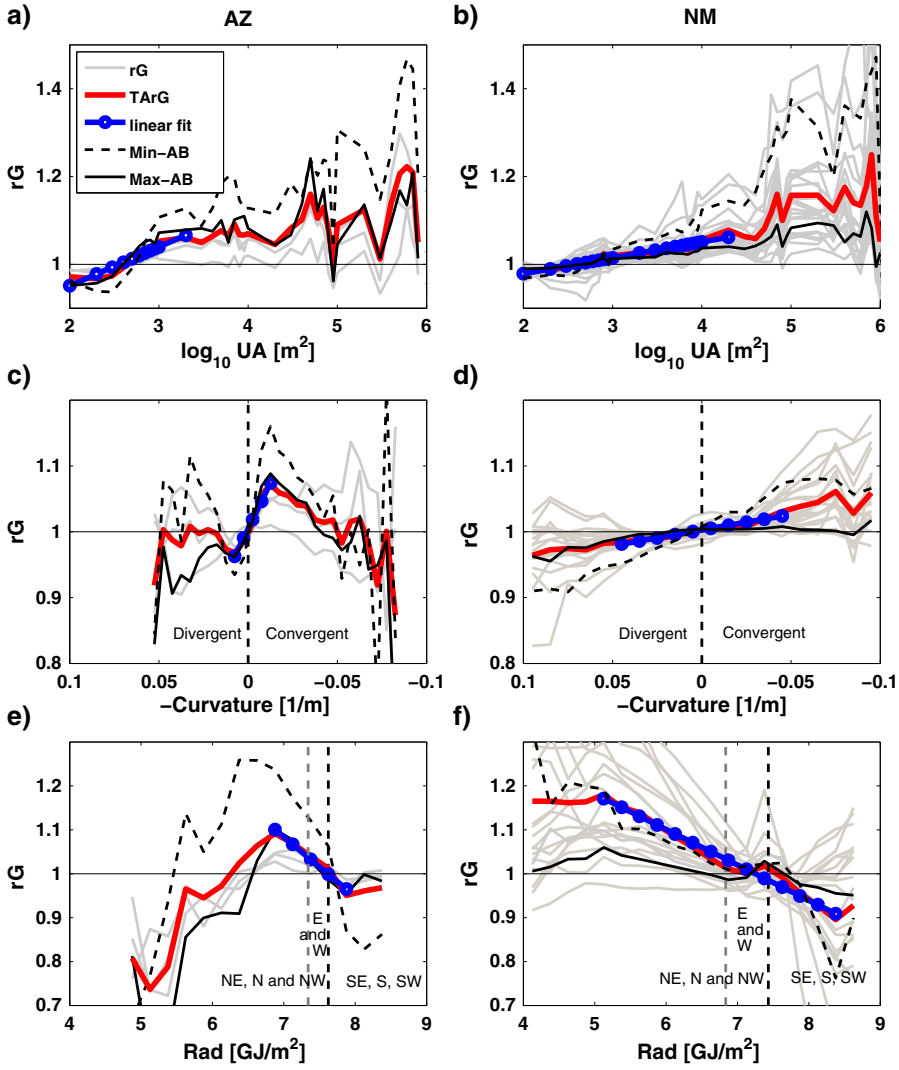

Figure 7. Relationships between *rG* (both daily and time-averaged *TArG*) and the three topographic variables at the AZ site using the binned and average data: (a) *rG* versus *UA*, (c) *rG* versus *Curv* and (e) *rG* versus *Rad*. (b), (d) and (f) are the same as (a, c, e) for the NM site. In each plot, a linear regression equation is plotted for the *TArG* data, comprising >80% of the data points. The fitted parameters of the linear regression equations are provided in Table II. Data for Min-AB and Max-AB days are indicated with black solid and dashed lines, respectively. The thin black horizontal line in all plots indicates $rG = 1$. In (c) and (d), the vertical dashed line indicates $Curv = 0$. In (e) and (f), the dashed vertical black line indicates *Rad* of a flat surface, whereas the dashed vertical grey line indicates the lower *Rad* limit of E and W aspects.

the plots. In ridges, identified from the *S–UA* relation in Figure 4(a) with $\log_{10}UA < \sim 2.6$, (*S–UA* region I), the binned average *rG* values are consistently less than 1. In valleys and channels with a support $\log_{10}UA > \sim 2.6$ (*S–UA* regions II and III), *rG* is higher than 1. Furthermore, *rG* generally shows a higher sensitivity to *UA* in the Min-AB data, especially in the valleys and channels, reflected in the steeper *rG–UA* response. This may suggest a stronger control of *UA* on green biomass early in the growing season.

In the AZ site, all *rG–UA* relations are rather flat initially for $\log_{10}UA < \sim 2.5$ (ridge region) but then become steeper as *UA* grows larger up to a value of approximately $\log_{10}UA$ of 3 (see red line in Figure 7(a)). In the *S–UA* relation of the AZ basin, *UA* between 2.5 and 3 coincides with the ridge–valley transition and areas around the VH, where significant topographic convergence first occurs (see dashed vertical line in Figure 4(a)). The same *UA* also corresponds to a sign change in the *Curv–UA* plot (Figure 4(b)). We argue that the change in landscape morphology in the VH region alters subsurface and surface flow paths, providing more moisture for plant growth and leading to a steeper *rG–UA* relation (subsurface flow has been reported at the Sevilleta site (Gutiérrez-Jurado *et al.*, 2007)).

In the NM site, however, the divergence to convergence shift occurs far upstream of the VH (Figure 4(a,b)). As a result, an increase in *rG* with *UA* around the VH is not clearly observed. Furthermore, in the *rG–UA* relation in NM with a semilog scale, the increase in *rG* appears linear. For example, *rG* increases a similar amount between *UA* of 100 to 1000 m^2 and between 1000 and 10,000 m^2. This indicates that the sensitivity of the ecosystem to a unit increase of *UA* diminishes as *UA* becomes large. Therefore, the ridges are more sensitive to changes in *UA* than the unchannelled valleys, and channels are the least sensitive among the three geomorphic regions. Notice also that as *UA* increases, the binned *rG* values for a given *UA* become highly variable. We attribute this to the smaller sample size of *UA* bins in the channel region. Pixels with $UA > 10{,}000\ m^2$ ($\log_{10}UA > 4$) comprise only ~5% of

the data. When the sample size is small, heterogeneities along the channels can contribute to the high *rG* variability.

We quantify the *rG–UA*, *rG–Curv* and *rG–Rad* relations in the binned data between the two sites using linear regression. Relations for *rG–Curv* and *rG–Rad* are discussed in subsequent sections. In the linear regression analysis, we focus on the ridges and unchanneled valleys that contain the majority of the basin areas, within a *UA* range corresponding to 92.5% and 97% of the AZ and NM sites, respectively. These data ranges are defined as the *data dense regions* in our analysis. A linear relation in the form of $rG = a \log_{10}UA + b$ is fitted to the binned *TArG* and $\log_{10}UA$ pairs (blue line with circles in Figure 7(a,b)) in the data dense region. Table III presents the calculated regression parameters. The linear relations are statistically significant to a level of $p < 0.001$ and explain over 88% of the variability in the binned *TArG* data as a function of $\log_{10}UA$ (r^2 is 0.88 for AZ and 0.93 for NM). We found the slope of the linear fit approximately twice as large at the AZ site than that of the NM site. This could reflect the relatively larger increase in *rG* along the ridge-to-valley transition in the wetter AZ site.

Curvature control. The *rG–Curv* relations are plotted in Figure 7(c,d) for the AZ and NM sites. The dashed vertical line in both figures marks planar slopes ($Curv = 0$). Converging (diverging) morphologies begin to the right (left) of this line. The overall role of *Curv* can be directly seen in the figures. In diverging terrain ($Curv < 0$), *rG* is less than 1 ($rG \leq 1$), and in converging terrain ($Curv > 0$), *rG* is higher than 1 ($rG > 1$) in the majority of the days in both locations. This indicates that by using curvature, regions of below and above mean spatial biomass may be distinguished in these semiarid ecosystems.

Linear regression equations are fit for *TArG–Curv* pairs in Figure 7(c,d), encompassing the data dense curvature ranges (~90% of the data) with consistent trends for all days plotted. The linear relations are statistically significant ($p < 0.001$) and explain over 94% of the variability in the binned *TArG* data as a function of *Curv* (r^2 is 0.97 and 0.94 for the AZ and NM sites, respectively; Table III). Data outside this range are sparse and highly variable leading to more variable *rG–Curv* dependence. Interestingly, the gradient of the linear fit is 12 times as high for the AZ site ($a = 5.56$) than that of the NM site ($a = 0.47$), albeit for a narrower range of curvatures. This may indicate that similar to the case of *UA*, *Curv* has a more profound impact on biomass in the AZ site than the NM site. With respect to seasonality, we note that the *rG–Curv* relations are steeper for days with low biomass (Min-AB) than high biomass (Max-AB) conditions. This may imply that under the same regional climate, curvature (as in the case of *UA*) would play a more pronounced role on vegetation biomass earlier in the growing season.

It is important to note that there is a significant positive correlation between *UA* and *Curv*, as evident in Figure 4(b). To examine this further we calculated the pixel-by-pixel intercorrelations among all the topographic variables. We found the highest correlation between *Curv* and *UA* (0.65 and 0.499 for AZ and NM, respectively), whereas *Rad* was not significantly related to neither *UA* nor *Curv* (see Table IV). Geomorphically, the reason for the high correlation is that as the local landform changes from a diverging to a converging morphology, the total *UA* that drains to the location grows. This influence is more pronounced on hillslopes with relatively small *UA*s. This correlation can influence the *rG–Curv* relations reported in Figure 7(c,d), in the sense that the positive relation observed between *rG* and *Curv* could be due to an increase in UA only. Likewise, the *rG–UA* relation could be influenced by the *UA–Curv* correlation as well.

To investigate this dependence, we calculated the total and partial correlations of *rG*–$\log_{10}UA$ (holding *Curv* constant for the partial correlation) and *rG–Curv* (holding $\log_{10}UA$ constant for the partial correlation) on a pixel-by-pixel basis, for the data dense region (see Table IV). From this analysis, we found the following. First, the total *TArG*–$\log_{10}UA$ and *TArG–Curv* correlations on a pixel-by-pixel basis are rather small (0.22 and 0.14, respectively, for AZ, and 0.09 and 0.04, respectively, for NM) because of the high scatter in the data. Second, we found that holding *Curv* constant led to a smaller partial correlation between *UA* and *TArG* than the total correlation, suggesting some contribution of *Curv* on the *UA–TArG* total correlation. Interestingly, holding *UA* constant, the partial correlation of *Curv–TArG* is negligible (and insignificant, $p > 0.45$). This practically indicates that on a pixel-by-pixel basis, correlation between *Curv* and *TArG* is a result of the correlation between *Curv* and *UA*.

Despite this strong control of *UA* on the *Curv–TArG* relation, we argue that the role of curvature on vegetation productivity should still be examined as a separate variable than *UA*, especially on hillslopes, where rapid changes in local

Table III. Linear regression of the relation between *TArG* and three topographic indices ($\log_{10}UA$, *Curv* and *Rad*) for each field site, corresponding to the data dense regions of each variable in Figure 7.

	AZ			NM		
	$\log_{10}UA$	*Curv*	*Rad*	$\log_{10}UA$	*Curv*	*Rad*
a	0.0887	5.5665	−0.1355	0.036	0.474	−0.081
b	0.7737	1.0047	2.0324	0.906	1.003	1.585
r	0.9355	0.9871	−0.978	0.964	0.971	−0.987
r^2	0.875	0.974	0.956	0.929	0.943	0.974
p	0	0.0018	0.0039	0	0	0
%	92.5	81.9	96.4	97.0	89.0	99.4

a and *b* are model parameters ($y = ax + b$), *r* is the correlation coefficient, r^2 is the coefficient of determination, *p* is the significance level and '%' indicates the percentage of data within the topographic index range considered in the regression.

Table IV. Correlation between *TArG* and three topographic indices ($\log_{10}UA$, *Curv* and *Rad*) for each field site, on a pixel-by-pixel basis, and partial correlations of *TArG*–$\log_{10}UA$ (holding *Curv* constant) and *TArG*–*Curv* (holding $\log_{10}UA$ constant).

	AZ				NM			
	Pixel-by-pixel data				Pixel-by-pixel data			
	$\log_{10}UA$	*Curv*	*Rad*	*TArG*	$\log_{10}UA$	*Curv*	*Rad*	*TArG*
$\log_{10}UA$	1	0.650	−0.014	0.217	1	0.499	0.031	0.089
Curvature	0.650	1	0.006	0.139	−0.499	1	−0.005	−0.044
Rad	−0.014	0.006	1	−0.267	−0.031	0.005	1	−0.167
TArG	0.217	0.139	−0.267	1	0.089	0.044	−0.167	1
$\log_{10}UA$|*Curv*	—	—	—	0.169	—	—	—	0.078
Curv|$\log_{10}UA$	—	—	—	−0.004	—	—	—	−0.001

UA is typically controlled by the changes in the morphology of the landform (e.g. diverging/converging), which can be best represented by local curvature as it represents changes in both profile and plan form shape of the landscape (Moore *et al*., 1991).

Radiation control. *Rad* for the AZ and NM sites was estimated for the latitudes of 32°N and 34°N, respectively. Given the latitude and ranges of *S* and *Asp* at each site, *Rad* varies between ~5 and ~8.5 GJ/m^2 (2000 to 3400 mm of water equivalent) in the AZ site, and ~4 and ~9 GJ/m^2 (1600 to 3600 mm of water equivalent) in the NM site. Figure 7(e,f) shows the *rG–Rad* relations for each site using the bin-averaged data. The black dashed vertical line indicates *Rad* corresponding to a flat surface (Rad_{flat}). *Rad* to the right of this line corresponds to south (S) facing terrain. *Rad* to the left of this line corresponds to east, west and north (E, W and N) facing terrain. The grey dashed vertical line indicates the lower *Rad* limit of west and east aspects. The region to the left of the grey dashed line is occupied only by north-facing terrain. In north-facing terrain, *Rad* is most sensitive to changes in local *S*, leading to a wider range of *Rad* (Figure 7(e,f)).

For relatively high values of *Rad*, *TArG* decrease with *Rad* in both sites. In the AZ site, this negative dependence corresponds to the 6.75 to 8 GJ/m^2 range, covering approximately 96% of the landscape area (Figure 7(e)). Outside of this range, for smaller *Rad* values, *TArG* increases with *Rad*. At the NM site, the negative relationship between the binned *TArG* and *Rad* covers the 5–8.5 GJ/m^2 range (~99% of the data). All 22 *rG–Rad* relations plotted for daily data also show a consistent negative dependence to *Rad*, whereas their magnitudes vary. Another observation consistent in both sites is that in the majority of the days plotted, $rG < 1$ for south-facing terrain (S, SE, SW), *rG* is close to 1 for east and west facing and $rG > 1$ for north-facing terrain. Notice that for both sites, similar to the case of *UA* and *Curv*, *rG* is most sensitive to *Rad* in the day of Min-AB. The linear regression equation fit to *rG–Rad* data in both sites in the data dense region of the *Rad* range ($p < 0.001$) explains over 96% of the variability in the binned *TArG* data as a function of *Rad* (r^2 is 0.96 and 0.97 for the AZ and NM sites, respectively; Table III). The gradient of the linear regression is ~50% steeper in the AZ site, suggesting a stronger sensitivity of ecosystem productivity to *Rad* at this site.

When the full range of *rG* response with *Rad* is considered, a local maximum of *rG* can be seen in the daily and time-averaged binned data at both sites on north-facing aspects. A maximum of vegetation cover at intermediate values of solar radiation exposure was predicted by Ivanov *et al*. (2008) using a numerical model. Ivanov *et al*. (2008) argued that this peak emerges from two limitations: 'radiation excess' for high values of *Rad* and 'rain insufficiency' for steep north-facing slopes, both leading to elevated plant water stress and reduced growth. Rain insufficiency was related to smaller rainfall projection area as *S* increases. In our field sites, in addition to rain insufficiency, steep terrain can also lose soil moisture laterally, as illustrated by Gutiérrez-Jurado *et al*. (2007) in the NM site.

The relations presented in this section show strong controls of upslope area, local curvature and solar radiation on relative plant productivity. In the next section, we explore if the strength of these topographic controls changes over time a result of seasonality and interannual fluctuations in climate.

Temporal variability. We calculate the correlation coefficient, *r*, between *rG* and each topographic index (r_{rG_UA}, r_{rG_Curv} and r_{rG_Rad}) for each day of the available data in the data dense ranges of each topographic variable (i.e. data used in the *TArG* regression lines in Figure 7). Correlations are presented for the bin-averaged data (Figure 8(c,d)) as used in Figure 7 and for pixel-by-pixel data (Figure 8(e,f)). The mean spatial NDVI and biomass for each day are presented in Figure 8(a,b) for reference.

The correlation coefficients are higher for the bin-averaged data (Figure 8(c,d)) than that for the individual pixel data (Figure 8(e,f)), as binning and averaging eliminate the variability around the mean of each bin value. Consistent with Figure 7, daily *rG* is positively related to *UA* and *Curv*, and negatively related to *Rad*. These calculations suggest that *r* varies with time. In the NM site, sometimes changes in $r_{rG–UA}$ and $r_{rG–Curv}$ are in synchrony. This may indicate coincidence of the influence of lateral water redistribution in the landscape at the local and catchment (e.g. channel network) scales.

In NM, *rG* depends negatively on *Rad* in all the data plotted, except for the data corresponding to 4/9/92, which shows a

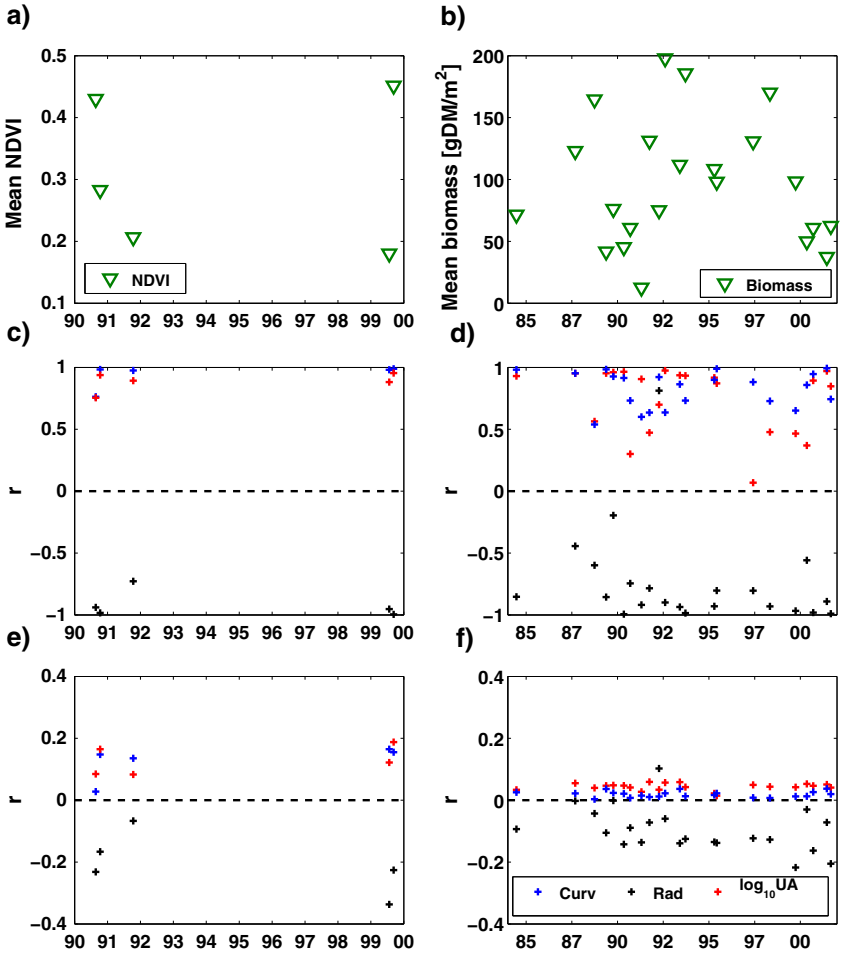

Figure 8. Regression analysis of the dependence of *rG* on *UA*, *Curv* and *Rad* for the AZ site: (a) time series of mean vegetation normalized difference vegetation index (NDVI); (c) correlation coefficients calculated for the binned data; (e) correlation coefficients calculated for the local pixel data; (b), (d) and (f) are the same as (a, c, e) for the NM site. Note that in (b), calculated biomass was used instead of NDVI.

positive *Rad* dependence. This could result from moisture accumulated during a particular wet winter, leading to a spring greening of the landscape (Notaro *et al.*, 2010). At the Bronco Well weather station in the SNWR, the cumulative precipitation between October 1991 and the end of March 1992 was 132 mm. The 18 year-mean precipitation for this site in the same period is 95 mm. It can be argued that at this site, the overall higher soil moisture across the landscape in the spring of 1992 led to enhanced plant productivity in areas where *Rad* is locally high.

Combined effects of lateral redistribution and evapotranspiration on ecosystem productivity. In the aforementioned analysis, we investigated *rG* relative to a single variable. Yet, lateral moisture redistribution, controlled by *UA* and *Curv*, and local evapotranspiration, driven by *Rad*, affect soil moisture patterns simultaneously (e.g. Western *et al.*, 1999) and consequently could have an impact on vegetation patterns. This can be analysed with a multivariate linear regression of *rG* as a function of the three topographic indices. We carried out such regression on a pixel-by-pixel basis for the data dense region using the time-averaged field of *rG*, *TArG*, and present the results in Table V. On a pixel-by-pixel basis, due to the high spatial variability of *TArG*, the relation between *TArG* and the topographic variables is weak: the coefficients of determination of the multivariate linear regressions are 0.12 and 0.04 for AZ and NM, respectively. The coefficients of the regression indicate that *Rad* and $\log_{10}UA$ have a stronger impact on *TArG* than *Curv* because although all coefficients are of the same order of magnitude, the range of the values of *Curv* is 100 times smaller than that of $\log_{10}UA$ or *Rad*.

Table V. Multiple linear regression of the relation between *TArG* and topographic indices ($\log_{10}UA$, *Curv* and *Rad*) for each field site, on a pixel-by-pixel basis and on a bin-averaged basis for AZ.

	AZ	NM	AZ
	Pixel by pixel	Pixel by pixel	Binned
b	1.5855	1.4886	1.9515
$a_{\log_{10}UA}$	0.0471	0.0385	0.5000
a_{Curv}	0.0271	−0.0328	2.5268
a_{Rad}	−0.0932	−0.0823	−0.1512
r	0.3420	0.1917	0.7960
r^2	0.1169	0.0367	0.6336

a_i and b are model parameters ($TArG = a_{\log_{10}UA} \log_{10}UA + a_{Curv} Curv + a_{Rad} Rad + b$), r is the correlation coefficient and r^2 is the coefficient of determination.

Next, to test whether or not binning the data would improve the explaining power of a multiple regression, we bin-averaged the pixel data on a 3D matrix for the AZ data set, where each axis of the matrix corresponds to each topographic index, binned concurrently on the basis of the bin range constraints defined for Figure 7 for each topographic index. This analysis is not conducted for NM because of the problems with binning the data with high variability and varying cell resolutions. The results are provided in Table V. With binning and averaging of the data, the explaining power of the multiple regression of *TArG* improves significantly. Its coefficient of determination is 0.63 (compared with 0.12 of the pixel scale multiple regression). Interestingly, 0.63 is smaller than the coefficient of determinations reported on the single-variable regressions (Table III). The reason for this is arguably that in the single-variable regression, we average out some of the variability preserved in the 3D binned data set.

Besides the multiple regression analysis, a more direct way of exploring the combined effects of more than one topographic variable in the ecosystems can be to examine the *rG–Rad* relations in different geomorphic regions identified along the *UA* gradient (Figure 9(a,b)). As with the multivariate linear regression, we limit the analysis to *TArG*, as it exhibits the general response behaviour to topographic variables consistent with most individual days in the record. The analysis can be easily extended to individual days. In Figure 9, the grey regions are data sparse regions with $<10\%$ of the basin areas.

Figure 9(a,b) shows that the general negative relation between *TArG* and *Rad* is preserved among the three geomorphic regions in the data dense range in the middle of the plots. The figures also show three clearly separated *TArG–Rad* relations, with the lowest *TArG* values corresponding to ridges and the highest values to channels. Unchanneled valleys plot between the two end members. Higher *TArG* as a result of changes from ridge to valley morphology clearly shows the role of increased moisture input. In the NM site, for channels, *TArG* first shows an increase, followed by a decrease (and partly no change in the 6.5–7.5 GJ range) as a function of *Rad*. This reduced sensitivity to *Rad* in channels in NM could be an indication of higher moisture in the channels that drain a larger watershed area in the NM site than in the AZ site. At the whole landscape scale, the *TArG–Rad* relation of the basin is dominated by ridges. Even though *TArG* along the channels and valleys can be up to 20% as high, these locations only represent a small fraction of the basin.

To further emphasize the cumulative effects of *UA* and *Rad* on *TArG*, we present *TArG* as a function of both *Rad* and *UA* in Figure 10(a,b), including contour lines for *TArG*, which we call 'isolines of productivity'. The horizontal dashed line indicates the value of flat surface *Rad*. The isolines reveal interesting patterns within the boundaries of the data dense regions indicated by the rectangles. The figures clearly illustrate the maximum and minimum productivity regions in the landscape. Maximum productivity regions correspond to the regions with lower *Rad* and higher *UA* (bottom-right corners of the inset rectangles, valleys on north-facing aspects), and minimum productivity regions correspond to the opposite condition (top-left corners of the inset rectangles, south-facing ridges). Beyond the data dense regions, as *UA* grows, higher *TArG* can be observed regardless of aspect. The relatively parallel isolines of productivity show the combinations of *Rad* and *UA* that result in equal *TArG*. This indicates that equal productivity regions on the landscape can connect landforms where *Rad* increase with *UA*. The slope of an isoline of productivity (between *Rad* and *UA*) would indicate the efficiency of moisture production of *UA*. The higher the slope of an isoproductivity line (i.e., the AZ site), the higher the amount of moisture an incremental increase of *UA* would bring to the location. To compensate the moisture increase, a higher *Rad* would be needed to keep *rG* constant. Note that in NM where rain is less, the isolines are further apart.

SUMMARY AND CONCLUSIONS

In this study, we examine the spatial variability of vegetation biomass, described with a relative greenness index, in relation to landscape morphology in select days corresponding to the growing season in two study sites located in southeastern Arizona and central New Mexico. We focus first on the differences in vegetation biomass variability in different

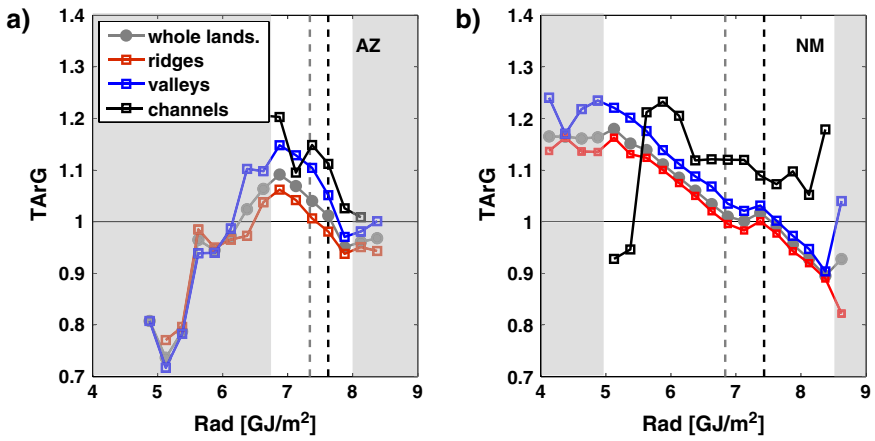

Figure 9. Relationship between *TArG* and *Rad* for ridges, valleys and channels. A vertical dashed line indicates *Rad* of a flat surface, whereas a dashed grey lines indicate the lower *Rad* limit of E and W aspects.

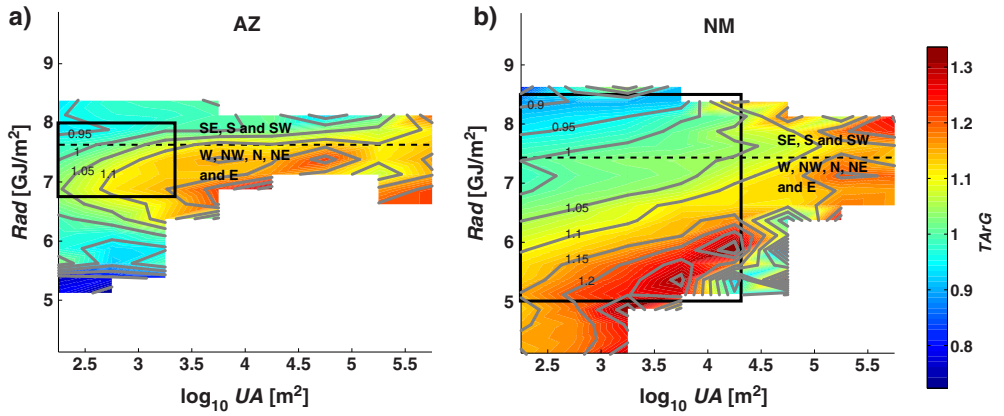

Figure 10. *TArG* as a function of both *Rad* and $\log_{10}UA$. A dashed line indicates *Rad* corresponding to a flat surface. Contour lines indicate 0.05 *TArG* increments. The dense regions defined for the linear regressions in Figure 7(a,e) (AZ) and 7(b,f) (NM) are indicated with a black rectangle. More than 90% of the terrain is represented within these rectangles.

morphologies (ridges, unchanneled valleys and channels). Second, we relate changes in relative vegetation biomass to selected topographic indices of upslope area (*UA*), local curvature (*Curv*) and local annual direct clear-sky radiation (*Rad*). The following are the major findings of this study:

- The shape of the rfd of *rG* in space is strongly correlated with the spatial mean (NDVI or biomass) at the landscape scale, with wetter periods (higher biomass, Max-AB) leading to a bell-shape form and drier periods (lower biomass, Min-AB) registering a greater spatial variability and multiple peaks in the rfds of the NM site.
- The rfd of *rG* shows differences among three geomorphic process domains (ridges, unchannelled valleys and channels), both in the shape and the distribution moments, with greater distribution mean corresponding to channels and higher skewness to ridges. In the AZ site with higher rainfall, these geomorphology-driven differences in the rfds are consistent among *TA–rG*, Min-AB and Max-AB cases. In the NM site, the role of geomorphology becomes less critical in the Min-AB and Max-AB cases.
- In both sites, under a low mean spatial vegetation cover, the variability and the range of *rG* increases everywhere in the landscape (compare Min-AB and Max-AB in Figure 6). Whereas the *rG* differences could be greater across the landscape, the absolute differences of biomass would be small compared with high spatial mean cover conditions. Therefore, the *rG* distributions should be evaluated with the spatial mean cover conditions on a seasonal basis.
- We observe nearly linear relations between the bin-averaged *TArG* and three topographic indices: $\log_{10}UA$ (positive), *Curv* (positive) and *Rad* (negative). These relations arise because of the modulation of moisture by the form of the terrain, which directs water towards depressions (high *Curv* and *UA*) and away from ridges (negative *Curv* and low *UA*) and which impacts water losses to evapotranspiration by controlling the solar radiation incidence.
- An analysis on the total and partial correlations between *TArG* and the topographic variables at the pixel scale revealed that the correlation between *TArG–Curv* is mostly due to the effect of *UA* on *TArG* through the intercorrelation between *UA* and *Curv*.
- Multivariate linear regressions at the pixel scale result in small coefficients of determination. Coefficients of determination significantly improve when data are binned in a multidimensional matrix, whereas the value is significantly lower than when a linear regression is performed using a single topographic variable at the time.
- The joint evaluation of the *UA* and *Rad* controls on *TArG* leads to the concept of equal plant productivity regions on the landscape. When the *Rad–UA* relationship is known for a given *rG*, this may be used for land use planning and predicting ecosystem response.

These findings shed light on spatial patterns of vegetation that can be explained with topographic indices and can be useful in ecosystem management, provide metrics to test distributed ecohydrology models and offer ideas for the downscaling of coarse-scale satellite vegetation observations to a finer DEM scale, conditioned on catchment geomorphology.

ACKNOWLEDGEMENTS

We acknowledge the support of NSF through the grants EAR-0963858 (Istanbulluoglu) and NSF EAR 0642550 (Bras). We are thankful for the Kendall data provided by the Southwest Watershed Research Centre (SWRC) and by the Sevilleta Long Term Ecological Research Programme. The authors would also like to thank two anonymous reviewers for their valuable comments and suggestions that eventually lead to an overall improvement of this manuscript.

APPENDIX

Estimation of incident shortwave radiation incident on the terrain (R_d)

Solar radiation is absorbed and scattered as it crosses the Earth's atmosphere. Assuming a solar constant at the top of the atmosphere, R_o, we can estimate the solar radiation reaching a surface normal to the sun, at the ground level, R_{gl}, with

$$R_{gl} = R_o e^{-n(0.128-0.054\log_{10}m)m} \quad \text{(A1)}$$

where $R_o = 1353\ \text{W/m}^2$; m is the optical air mass, $m = \boldsymbol{csc}(h_\oplus)$, where $h_\oplus$ is the solar altitude or angle of the Sun's beam with respect to an observer's horizon plane; and n is a turbidity factor of air ($n = 2$ for clear air) (Bras, 1990). Equation (A1) takes into account the length of the trajectory of a solar ray through the atmosphere before reaching the ground at a given location of the planet.

The amount of R_{gl} incident on the terrain, R_d, taking into account terrain inclination and aspect, α_∇ and β_∇, is estimated by means of the solar angle of incidence, $\varphi_{\oplus\nabla}$, defined as the angle between the Sun's beam and the normal to the surface:

$$R_d = R_{gl}\cos\left(\varphi_{\oplus\nabla}\right) \quad \text{(A2)}$$

The solar angle of incidence ($\varphi_{\oplus\nabla}$) is calculated as follows:

$$\cos\varphi_{\oplus\nabla} = \cos\alpha_\nabla \sin h_\oplus + \sin\alpha_\nabla \cos h_\oplus \cos\left(\phi_{\oplus az} - \beta_\nabla\right) \quad \text{(A3)}$$

where β_∇ is defined as the angle between the direction the surface faces and the geographic North, clockwise from the geographic North, that is, β_∇ is 180° for a south-facing slope, and $\phi_{\oplus az}$ is the Sun's azimuth.

The surface's inclination and aspect, α_∇ and β_∇, are obtained from the geometry of the terrain; solar latitude and the Sun's azimuth, $h_\oplus$ and $\phi_{\oplus az}$, are calculated on the basis of the time of the day, day of the year and local latitude, ϕ, as follows:

$$\sin h_\oplus = sin\phi \sin\delta_\oplus + \cos\phi\cos\delta_\oplus\cos\tau_\oplus \quad \text{(A4)}$$

$$\phi_{\oplus az} = \tan^{-1}\left[\frac{\sin\tau_\oplus}{\tan\delta_\oplus\cos\phi - \sin\phi\cos\tau_\oplus}\right] \quad \text{(A5)}$$

where $\delta_\oplus$ is the declination of the Sun (angular distance between the celestial equator plane and the Sun, measured along the hour circle, positive when the Sun lies north of the Earth's equator) and $\tau_\oplus$ is the hour angle of the Sun (angular distance between the planes of the meridian and the Sun's hour circle) (Eagleson, 2002).

In the calculation of $h_\oplus$, we only consider positive values because negative values indicate that the sun is below the horizon. For numerical stability, we set the threshold at $h_\oplus > 0.25°$. In the calculation of $\phi_{\oplus az}$, one must check that the value obtained with Equation (A5) corresponds to the correct angle, given that $\tan\phi_{\oplus az} = \tan(\phi_{\oplus az} + 180°)$ but $\phi_{\oplus az} \neq \phi_{\oplus az} + 180°$.

The sun's declination $\delta_\oplus$ is approximated by

$$\delta_\oplus = 23.45\cos\left[\frac{365}{360}(172 - \text{JDay})\right] \quad \text{(A6)}$$

where *JDay* is the Julian day of the year.

The sun's hour angle $\tau_\oplus$ is a function of the hour of the day, and T_{ST} is the standard time in the zone of the observer counted from midnight (in hours):

$$\tau_\oplus = 15(T_{ST} + 12 - \Delta T_{ST}), \text{if } T_{ST} < 12 + \Delta T_{ST} \quad \text{(A7a)}$$

$$\tau_\oplus = 15(T_{ST} - 12 - \Delta T_{ST}), \text{if } T_{ST} > 12 + \Delta T_{ST} \quad \text{(A7b)}$$

where ΔT_{ST} is the time difference between standard and local meridian. In this work, we assume that ΔT_{ST} is negligible.

REFERENCES

Beven KJ, Kirkby NJ. 1979. A physically based variable contributing area model of basin hydrology. *Hydrological Sciences Bulletin* **24**: 43–69.

Blöschl G, Grayson R. 2001. Spatial observations and interpolation. In *Spatial Patterns in Catchment Hydrology*, 1st edn, Brayson R, Blöschl G (eds). Cambridge University Press: Cambridge.

Bogaart PW, Troch PA. 2006. Curvature distribution within hillslopes and catchments and its effect on the hydrological response. *Hydrology and Earth System Sciences* **10**: 925–936.

Bonan G. 2008. *Ecological climatology, concepts and applications*, 2nd edn. Cambridge University Press: Cambridge, United Kingdom.

Bras RL. 1990. *Hydrology, An Introduction to Hydrologic Science*, 1st edn. Addison-Wesley Publishing Company: United States of America.

Collins DBG, Bras RL, Tucker GE. 2004. Modeling the effects of vegetation–erosion coupling on landscape evolution. *Journal of Geophysical Research* **109**: F03004.

Dunne T, Black RD. 1970. Partial area contributions to storm runoff in a small New England watershed. *Water Resources Research* **6**: 1296–1311.

Dunne T, Moore TR, Taylor CH. 1975. Recognition and prediction of runoff-producing zones in humid regions. *Hydrological Sciences Bulletin* **20**: 305–327.

Eagleson PS. 2002. *Ecohydrology: Darwinian Expression of Vegetation Form and Function*. Cambridge University Press: Cambridge.

Florinsky IV, Kuryakova GA. 1996. Influence of topography on some vegetation cover properties. *Catena* **27**: 123–141.

Gasparini NM, Tucker GE, Bras RL. 2004. Network-scale dynamics of grain-size sorting: implications for downstream fining, stream-profile concavity, and drainage basin morphology. *Earth Surface Processes and Landforms* **29**: 401–421. DOI: 10.1002/esp.1031

Gutiérrez-Jurado HA, Vivoni ER. 2011. Ecogeomorphic expressions of an aspect-controlled semiarid basin: I. Topographic analyses with high resolution data sets. *Ecohydrology*. DOI: 10.1002/eco.280

Gutiérrez-Jurado HA, Vivoni ER, Harrison JF, Guan H. 2006. Ecohydrology of root zone water fluxes and soil development in complex semiarid rangelands. *Hydrological Processes* **20**: 3289–3316.

Gutiérrez-Jurado HA, Vivoni ER, Istanbulluoglu E, Bras RL. 2007. Ecohydrological response to a geomorphically significant flood event in a semiarid catchment with contrasting ecosystems. *Geophysical Research Letters* **34**: L24S25. DOI: 10.1029/2007GL030994

Hack JT, Goodlett JC. 1960. Geomorphology and forest ecology of a mountain region in the central Appalachians. *Professional paper U.S. Geological Survey*.

Hidalgo JCG, Pellicer L, Lopez MV. 1990. Spatial distribution patterns of morphogenetic processes in a semiarid region. In *Vegetation and Erosion, Processes and Environments*, Thornes J (ed.). John Wiley & Sons: New York; 399–417.

Holifield CD, McElroy S, Moran MS, Bryant R, Miura T, Emmerich WE. 2003. Temporal and spatial changes in grassland transpiration detected using Landsat TM and ETM + imagery. *Canadian Journal of Remote Sensing* **29**: 259–270.

Howard AD. 1980. Thresholds in river regimes. In *Thresholds in Geomorphology*, Coates DR, Vitek JD (eds). Allen & Unwin: London; 227–258.

Hwang T, Band L, Hales TC. 2009. Ecosystem processes at the watershed scale: extending optimality theory from plot to catchment. *Water Resources Research* **45**. DOI: 10.1029/2009WR007775

Istanbulluoglu E, Bras RL. 2005. Vegetation-modulated landscape evolution: effects of vegetation on landscape processes, drainage density, and topography. *Journal of Geophysical Research* **110**: F02012.

Istanbulluoglu E, Yetemen O, Vivoni ER, Gutiérrez-Jurado HA, Bras RL. 2008. Ecogeomorphic implications of hillslope aspect: inferences from analysis of landscape morphology in central New Mexico. *Geophysical Research Letters* **35**: L14403.

Ivanov VY, Bras RL, Vivoni ER. 2008. Vegetation-hydrology dynamics in complex terrain of semiarid areas: 2. Energy-water controls of vegetation spatiotemporal dynamics and topographic niches of favorability. *Water Resources Research* **44**: W03430. DOI: 10.1029/2006WR005595

Kirkby MJ, Atkinson K, Lockwood JG. 1990. Aspect, vegetation and erosion on semiarid hillslopes. In *Vegetation and Erosion*, Thornes JB (ed.). Wiley: Chichester; 25–39.

Knoepp JD, Swank WT. 1998. Rates of nitrogen mineralization across an elevation and vegetation gradient in the southern Appalachians. *Plant and Soil* **204**: 235–241. DOI: 10.1023/A:1004375412512

Knoepp JD, Vose JM, Swank WT. 2008. Nitrogen deposition and cycling across an elevation and vegetation gradient in southern Appalachian forests. *International Journal of the Environment Studies* **65**: 391–410. DOI: 10.1080/00207230701862348

Larcher W. 2003. *Physiological Plant Ecology, Ecophysiology and Stress Physiology of Functional Groups*, 4th edn. Springer-Verlag: Germany.

Montgomery DR. 1999. Process domains and the river continuum. *Journal of the American Water Resources Association* **35**: 397–410.

Moore ID, Grayson RB, Ladson AR. 1991. Digital terrain modelling in hydrology. *Hydrological Processes* **5**: 1.

Moore ID, O'Loughlin EM, Burch GJ. 1988. A contour-based topographic model for hydrological and ecological applications. *Earth Surface Processes and Landforms* **13**: 305–320. DOI: 10.1002/esp.3290130404

Muldavin E, Shore G, Taugher K, Milne B. 1998. A vegetation classification and map for the Sevilleta National Wildlife Refuge, New Mexico. Final report. New Mexico Natural Heritage Program and Sevilleta Long Term Ecological Research Program, Biology Department, University of New Mexico: Albuquerque, NM.

Notaro M, Liu Z, Gallimore RG, Williams JW, Gutzler DS, Collins S. 2010. Complex seasonal cycle of ecohydrology in the southwest united states. *Journal of Geophysical Research* **115**: G04034. DOI: 10.1029/2010JG001382

Nouvellon Y, Moran MS, Lo Seen D, Bryant R, Rambal S, Ni W, Bégué A, Chehbouni A, Emmerich WE, Heilman P, Qi J. 2001. Coupling a grassland ecosystem model with Landsat imagery for a 10-year simulation of carbon and water budgets. *Remote Sensing of Environment* **78**: 131–149.

Noy-Meir I. 1973. Desert ecosystems: environment and producers. *Annual Review of Ecology and Systematics* **4**: 25–51. DOI: 10.1146/annurev.es.04.110173.000325

Riveros-Iregui DA, McGlynn BL. 2009. Landscape structure control on soil CO2 efflux variability in complex terrain: scaling from point observations to watershed scale fluxes. *Journal of Geophysical Research* **114**: G02010. DOI: 10.1029/2008JG000885

Schwinning S, Sala OE, Loik ME, Ehleringer JR. 2004. Thresholds, memory, and seasonality: understanding pulse dynamics in arid/semi-arid ecosystems. *Oecologia* **141**: 191–193.

Sharon D. 1980. The distribution of hydrologically effective rainfall incident on sloping ground. *Journal of Hydrology* **46**: 165–188.

Shore GA, Gosz JR. 2002. Use of Landsat TM spectral vegetation indices for biomass/NPP Estimation. *Sevilleta Long Term Ecological Research Data Bank*; Albuquerque, NM. [Database]. Available: http://sev.lternet.edu/ (May 9 2007).

Sólyom PB, Tucker GE. 2004. Effect of limited storm duration on landscape evolution, drainage basin geometry, and hydrograph shapes. *Journal of Geophysical Research* **109**: F03012. DOI: 10.1029/2003JF000032

Svoray T, Karnieli A. 2010. Rainfall, topography and primary production relationships in semiarid ecosystem. *Ecohydrology*. DOI: 10.1002/eco.123

Tarboton DG, Bras RL, Rodriguez-Iturbe I. 1992. A physical basis for drainage density. *Geomorphology* **5**: 59–76.

Tarolli P, Dalla Fontana G. 2009. Hillslope-to-valley transition morphology: new opportunities from high resolution DTMs. *Geomorphology* **113**: 47–56.

Tucker GE, Bras RL. 1998. Hillslope processes, drainage density, and landscape morphology. *Water Resources Research* **34**: 2751–2764.

Western AW, Grayson RB, Blöschl G, Willgoose GR, McMahon TA. 1999. Observed spatial organization of soil moisture and its relation to terrain indices. *Water Resources Research* **35**(3): 1999.

Whiteman CD. 2000. *Mountain Meteorology, Fundamentals and Applications*. Oxford University Press: New York, NY.

Willgoose GR, Perera HJ. 2001. A simple model for saturation excess runoff generation using geomorphology, steady-state soil moisture. *Water Resources Research* **37**: 147–156.

Willgoose G, Bras RL, Rodriguez-Iturbe I. 1991. A coupled channel network growth and hillslope evolution model: 1. Theory. *Water Resources Research* **27**: 1671–1684.

Wobus C, Whipple KX, Kirby E, Snyder N, Johnson J, Spyropolou K, Crosby B, D Sheehan. 2006. Tectonics from topography: procedures, promise, and pitfalls. In *Tectonics, Climate and Landscape Evolution*, Willett SD, Hovius N, Brandon MT, Fisher DM (eds). GSA: Boulder, CO; 55–74.

Yetemen O, Istanbulluoglu E, Vivoni ER. 2010. The implications of geology, soils, and vegetation on landscape morphology: inferences from semi-arid basins with complex vegetation patterns in central New Mexico, USA. *Geomorphology* **116**: 246–263. DOI: 10.1016/j.geomorph.2009.11.026

Zevenbergen LW, Thorne CR. 1987. Quantitative analysis of land surface topography. *Earth Surface Processes and Landforms* **23**: 47–56.